Available online at www.sciencedirect.com

jmr&t Journal of Materials Research and Technology

www.jmrt.com.br

Original Article

Study and classification of the Crystallographic Orientation Distribution Function of a non-grain oriented electrical steel using computer vision system

Roberto Fernandes Ivo[a], *Douglas de Araújo Rodrigues*[a], *José Ciro dos Santos*[a], *Francisco Nélio Costa Freitas*[a], *Luis Flaávio Gaspar Herculano*[b], *Hamilton Ferreira Gomes de Abreu*[b], *Pedro Pedrosa Rebouças Filho*[a,*]

[a] *Programa de Pós-Graduação em Energias Renováveis, Instituto Federal de Educação, Ciência e Tecnologia do Ceará, Fortaleza, CE, Brazil*
[b] *Departamento de Engenharia Metalúrgica e de Materiais, Universidade Federal do Cearã (UFC), Fortaleza , CE, Brazil*

ARTICLE INFO

Article history:
Received 6 December 2017
Accepted 8 May 2018
Available online 19 September 2018

Keywords:
Electrical steel
Crystalline Orientation Distribution Function
Digital image processing
Pattern recognition

ABSTRACT

This article discusses a fast and efficient classification of non-grain oriented electrical steel and its electromagnetic efficiency based on the analysis of the images of the Crystalline Orientation Distribution Function (CODF). The study was carried out on samples of a non-grain oriented electrical steel, semi-processed with 1.28% silicon, cold rolled with thickness reductions of 50.0% and 70.0%, and annealed at 730 °C for 12 h. The material was also subjected to annealing heat treatment for grain growth at temperatures of 620 °C, 730 °C, 840 °C and 900 °C for 1, 10, 100 and 1000 min at each temperature. The database used was comprised of 32 images. The extractors Gray Level Co-occurrence Matrix (GLCM), Local Binary Patterns (LBP), Central Moments, Statistical Moments, and Hu's Moments were combined with the following classifiers: Bayes, k-Nearest Neighbor (kNN) with 1, 3, and 5 nearest neighbors, MultiLayer Perceptron (MLP) with two configurations, Support Vector Machines (SVM) with four different kernel types (linear, polynomial, radial basis function (RBF) and sigmoid). For all the using cases the method of partitioning data Hold Out. Measurements of precision, sensitivity, specificity and positive predictive values, as well as the confusion matrix were used to evaluate the classifiers. The SVM with polynomial using the GLCM extractor had the highest accuracy rate of 89.00%, specificity of 86.93%, sensitivity of 80.69% and positive predictive values of 80.34%. The time required for this combination, which was the best, was only 0.6 ms. The results showed that this approach generated a new methodology for the analysis of non-grain oriented electrical steels.

* *Corresponding author.*
E-mail: pedrosarf@ifce.edu.br (P.P. Rebouças Filho).
https://doi.org/10.1016/j.jmrt.2018.05.028

1. Introduction

There is an incessant search for highly efficient electrical devices with low magnetic losses [1,2]. Consequently, many researchers have turned their attention to electric steels to obtain such characteristics [3–5].

Electrical steels present excellent magnetic properties due to a higher silicon content in their chemical composition compared to ordinary steels. This increase in silicon contributes to higher electrical resistivity and low magnetic losses [6,7].

Electric steels are present, for example, in transformers and electric motors. In electric motors, the class of electrical steels are non-grain oriented (NGO) [8,9]. The microstructural characteristics of the NGO electrical steels are directly related to their electromagnetic performance, and their magnetic properties are independent of the direction considered, feature known as isotropy.

The literature states that the electromagnetic efficiency of NGO electrical steels is evaluated from magnetic hysteresis curves [9–13], microstructural state [14–18] or the crystallographic texture. Fig. 1 presents the microstructure, the Crystalline Orientation Distribution Function (CODF) and the hysteresis curve to characterize 1.28% silicon electrical steel with a 70.0% thickness reduction, cold rolled and annealed at 900 °C.

Magnetic losses are minimized when the grain present in the microstructure reach an optimal size. This ideal grain size is limited to 100 μm and 150 μm [13], which is when the material has a higher electromagnetic efficiency. The sizes of the grains are directly related to the treatments that the electric steel is submitted to and to the manufacturing processes.

The hysteresis curve has its own interpretation for the characterization, since it shows the amount of energy, during a total cycle, dissipated by the Joule effect. The measure of the internal area of the hysteresis curve of the material shows the portion of the electric energy consumed due to magnetic losses [10].

The texture represents the orientation distribution of the crystals which constitute the metallic materials such as electrical steels. A full description of the texture of electrical steels, requires the information concerning the planes, directions, and volume of each orientation present [19,20].

The characterization of the electrical steel texture can be through an analysis of the CODF. However, this characterization is an activity that requires very careful examination by an experienced professional to avoid any errors.

On the other hand several techniques of digital image processing (DIP) and pattern recognition have been employed in various fields of Materials Science to assist professionals and experts in their analytical activities. Optical microscopy studies are commonly used for the microstructural characterization and analysis of cast iron [21,22], for graphite density nodule calculations [23] and for the quantification of microstructures in metals using artificial neural networks.

The work of [18] carried out a computational study to classify the electromagnetic efficiency of non-grain oriented electrical steel through the microstructure analysis of the material using Computational Vision. As a complement to that work, this work studies and classifies the same material as [18]; however, now the analysis is based on the crystallographic texture of the electric steel.

The present work aims to present an analysis of the recrystallization electrical steel texture after the heat treatments for grain growth and to carry out a DIP based computational study to classify the texture of the electrical steel using CODF images. Also, the scientific basis for the interaction between the microstructure and the texture of the electric steel is explored.

2. Literature review

This section begins with a review of the literature on materials science and is followed by a review of the computational aspects.

2.1. *Material science review*

In this section we present a review of the literature on crystallographic texture, the CODF and the crystallographic texture in electric steel.

2.1.1. *Crystallographic texture*

Metals have polycrystalline structures formed by a large number of microcrystals. The way crystal orientations are distributed in a polycrystalline material is the crystallographic

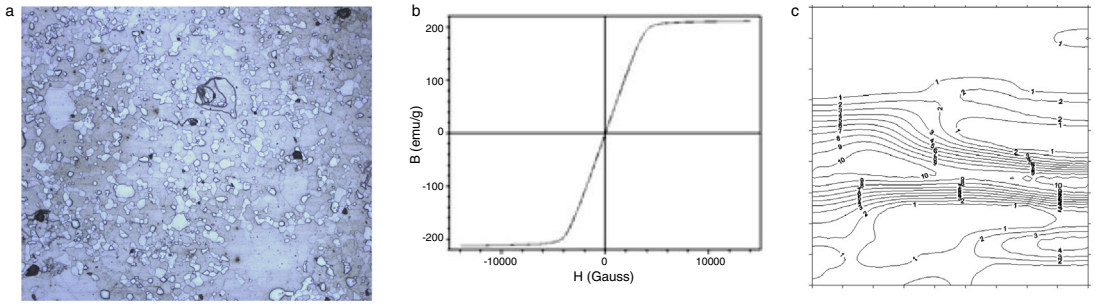

Fig. 1 – Characterization of the NGO electric steel with 1.28% of silicon with a thickness reduction of 70.0%, cold rolled, and annealed at 900 °C for 1000 min.

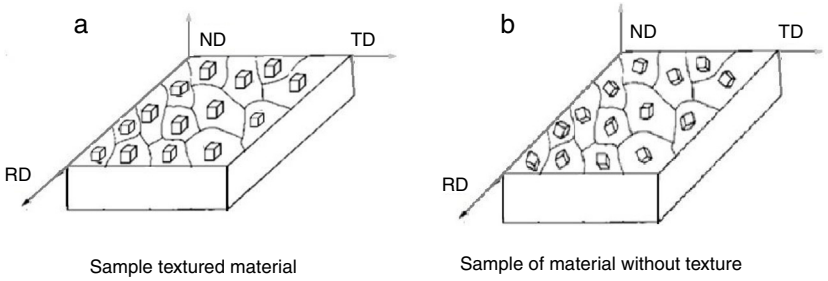

Fig. 2 – Crystallographic texture.

texture. A non-textured material is a material where the orientation of the crystals in the polycrystalline aggregate is totally random. Fig. 2a and b represent materials with crystallographic texture and no crystallographic texture, respectively.

Solidification, plastic deformation and recrystallization in metals lead to the formation of a preferred orientation. In this orientation, certain crystallographic axes are defined geometrically in relation to the macroscopic directions of the metallic body.

The texture can be represented by an orientation of the crystals considered ideal, which is called the component. For a laminated sheet, the component is represented by a crystalline plane (*hkl*), which is parallel to the plane of the sheet, and by the direction [*uvw*] belonging to the plane (*hkl*), which is parallel to the rolling direction (RD). Consequently, the orientation of the crystals with respect to the RD, transverse direction (TD) and normal direction (ND) axes of the plate is established.

A more complete description of texture requires data about the distribution of its crystallographic orientations. The Crystalline Orientation Distribution Function is used to describe the plans, directions, and volume of each orientation present. In addition, the CODF characterizes the probability density of finding certain orientations in a sample of a steel plate, for example.

The DF of the crystalline orientations is determined by a relation between the RD of the sample, the TD and the ND with the axes of the unit cell (x, y, z). This relation is through the angles of Euler (ϕ_1, ϕ, ϕ_2).

The CODF is represented in sections of constant ϕ, as shown in Fig. 3. Each section is a sequence of significance levels that are interpreted by the abacus as a whole. An example of this abacus is shown in Fig. 4.

According to Bunge [24], the $\phi_2 = 45°$ section has the main information about the crystallographic planes and directions

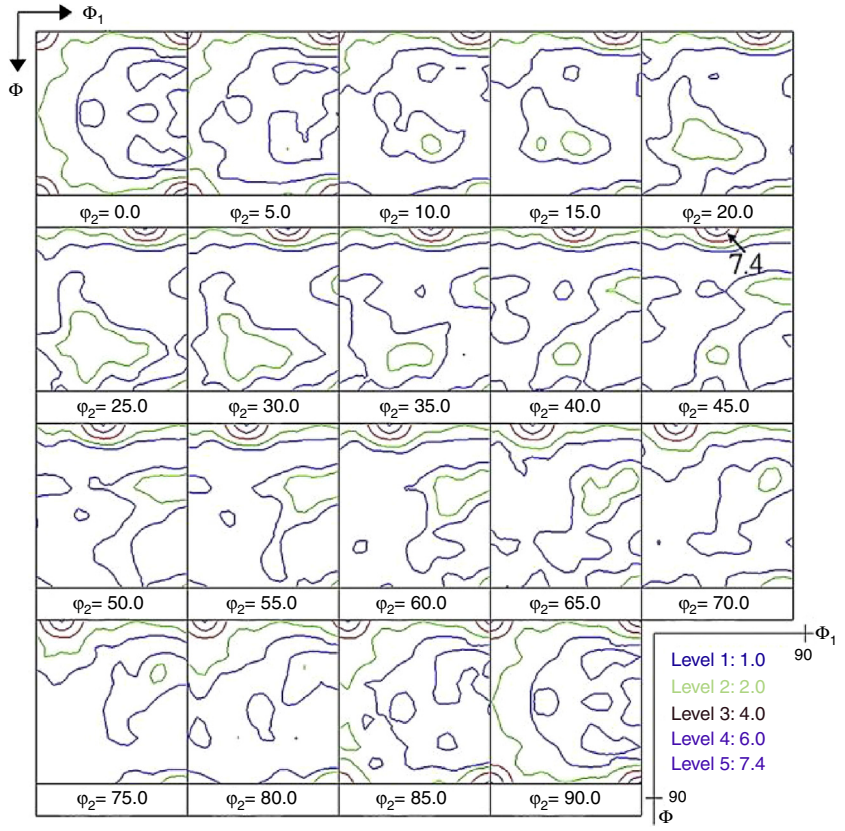

Fig. 3 – CODF of the annealed copper strip. [25].

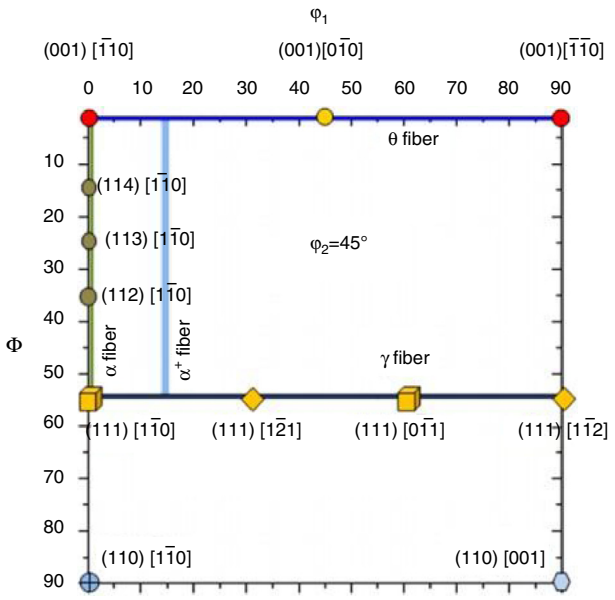

Fig. 4 – Abacus showing the main planes and directions for the $\phi_2 = 45°$ section along with the fibers α, γ and θ [26].

of electric steel. These planes and directions can be interpreted through the abacus as shown in Fig. 4, with these three characteristic fibers α (DR), γ (DN) and θ (DT). The fiber α is of the family of directions $\langle 110 \rangle$ parallel to the rolling direction (RD); since the fiber γ is of the family of directions $\langle 111 \rangle$ parallel to the normal direction (ND) and to the rolling direction (RD); and fiber θ to family of directions parallel to the normal direction (ND) and the rolling direction (RD).

The crystallographic texture in metallic materials may be due to several factors. Among the most important are the texture resulting from the plastic deformation and the texture resulting from the recrystallization of the metal. When a deformed metal is subjected to an annealing heat treatment, recovery and/or recrystallization may occur. The occurrence of recrystallization may generate crystallographic orientations utterly different from those caused by the deformation. This recrystallization can either lead to the absence of texture or to the development of powerful texture components or simply not alter the texture of the deformation.

2.1.2. *Crystalline Orientation Distribution Function*

X-ray diffraction and Electron Backscatter Diffraction (EBSD) techniques are distinct ways to determine the Crystalline Orientation Distribution Function.

The X-ray diffraction (XRD) technique evaluates the crystallographic texture in a macro manner, that is, it takes into account a considerable volume of crystals of the material. The XRD technique obtains pole figures, based on stereographic projections. An X-ray beam strikes a sample, and part of the reflected radiation is collected by a detection system that processes the signal and then provides the pole figures that will give rise to the CODF. The incidence of radiation on the sample occurs at the same rate as the diffraction angle 2θ increases.

The EBSD technique is used when the texture shows few crystals or even a single crystal. This procedure is based on the acquisition of images through scanning electron microscopy (SEM).

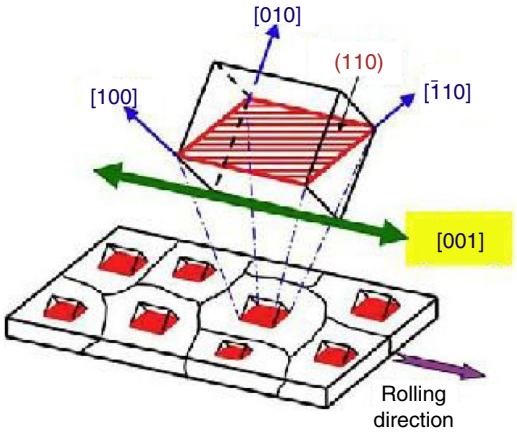

Fig. 5 – Goss texture formation [28].

In addition to CODF, the crystallographic texture of a metallic material can also be evaluated through the inverse pole figures. In most cases, they are calculated through the conventionally obtained CODF, but can also be calculated directly by the diffraction methods already mentioned. Through the inverted pole figures it is possible to obtain the numerical values on the level curves that establish the intensity of the direction.

2.1.3. *Crystallographic texture of electrical steels*

One of the major challenges for the producers of NGO electrical steels is to obtain a crystallographic texture that is favorable to the magnetic properties. This can be done by decreasing the fraction of undesirable texture components such as [111]//ND and increasing the percentage of favorable components such as [100]//TD and [100]//RD.

In pursuit of the best texture for electrical steels, Goss [27] has developed and patented a method of manufacturing oriented grain steels which confer excellent magnetic permeability in the rolling direction as a result of the formation of a strong texture (110)[001]. This texture is called the Goss texture component and Fig. 5 illustrates its formation.

The production process developed by Goss is used to manufacture NGO electric steels, and requires that the machines and equipment producing such material be mounted so that the magnetic flux is parallel to the rolling direction of the sheet.

2.2. *Computational review*

This section presents a review of the literature on attribute extractors, pattern recognition, as well as the confusion matrix and evaluation metrics.

2.2.1. *Feature extraction*

Relevant information about an image, such as shape and texture, is obtained through attribute extractors. These attributes highlight the differences and similarities between the objects present in the images [29]. They are stored in a vector and are usually input data for a classifier [30].

The Central Moment extractor performs a description of the shape of the objects present in the image or its regions. This representation is possible due to its function of translational invariance. For the construction of the attribute vectors, this extractor uses the center of gravity of the object as the reference point. Despite its invariance to translation, this extractor is dependent on the scale and rotation of objects [31,32].

Statistical Moments perform the extraction based on the distribution of gray levels present in the image under analysis. The statistical distribution of these gray levels is obtained from the histogram of the input image [33].

One of the main problems present in the classification of an object is the variation of the characteristics of scale or rotation. Such questions are solved using the Hu Moments extractor [33]. In this case the extraction is independent on the orientation, size, and position of the object. Mathematical equations are responsible for constructing the attribute vector. In this way, it is possible to describe two-dimensional geometric figures based on two-dimensional invariants [34–36].

Haralick et al. [37] stated that the texture of an image is an innate property of virtually all surfaces. The texture has essential information about the structural arrangement and its relation to the surrounding environment. Haralick proposed an extraction based on the texture of the image. This extractor uses the resources derived from the Gray Level Co-occurrence Matrix (GLCM) calculations that serve as the basis for the preparation of the statistical measures known as Haralick Descriptors [38,39].

Ojala et al. [40] proposed a local Binary Patterns (LBP) extractor. In this extractor, each pixel in the image is assigned a label from a local adaptive thresholding. Consequently, there is the construction of a histogram and the description of the texture. At first, the 3×3 kernel was used to perform the thresholding. However, as it became necessary to describe textures of several scales the LBP operator had to work with different kernels.

2.2.2. *Pattern recognition*

Pattern recognition makes use of classifiers to recognize structures or related characteristics. Applications that use pattern recognition are quite numerous, and can be used for facial recognition [41], in the field of medicine [42–44] and in materials science [45,46]. The main classifiers present in the literature are the Bayesian, Support Vector Machines, Optimum Path Forest, Multilayer Perceptron and k-Nearest Neighbors.

The Bayesian classifier uses a statistical approach to learning, and in this case, it assumes that the samples follow a probability distribution. In this classifier, a sample is determined to belong to a class if this class is predicted to be the most likely, that is, the class that received most of the probabilities. The concepts of a priori and a posteriori probability are used, to define, respectively, initial and posterior estimates for these calculations [47,48].

Support Vector Machines (SVM) is a supervised learning algorithm used for classification, and regression analysis [49,50]. The basis of the SVM is the theory of Statistical Learning Theory, which was developed by Vapnik from studies started in [51]. The classifier presents a series of elements used to obtain a suitable classifier. SVM is useful both for classifying linearly separable and non-linear datasets [52]. In the second case, it is common to use other kernels, for example, linear, polynomial, radial basis function (RBF) and sigmoid.

The Optimum Path Forest (OPF) was developed by Papa et al. [53], and has already been used in various applications [54–56]. The theory of graphs is the foundation for supervised learning of the classifier. The OPF establishes a process of competition between some reference samples, determined during training in search of partitioning the graph in a forest of optimal paths.

The Multilayer Perceptron (MLP) is an artificial multilayer neural network aimed at solving problems whose patterns are non-linearly separable. Its structure is composed of an input layer, one or more hidden layers and an output layer [57]. The formation of the hidden layers is by neurons that influence the high order statistical acquisition. The network connection weights measure the degree of correlation between the activity levels of the neurons they connect. The synaptic weights are adjusted through a network training algorithm.

k-Nearest Neighbors (kNN) is a supervised learning algorithm, introduced by [58–60]. The principle of this classifier is to find the κ samples closest to the unknown samples and use them to classify an unknown example. kNN requires little effort in the training stage. In contrast, the computing cost for labeling an unknown sample is relatively high. The number of neighbors is the parameter in kNN [61].

2.2.3. *Confusion matrix and evaluation metrics*

The confusion matrix contains information about actual and predicted classifications made by a classification system. Thus, it is a valid tool to evaluate the efficiency of a computational classifier. This matrix validates supervised learning. The main diagonal of the confusion matrix indicates the correct answers, and the other components correspond to the classification errors.

The main diagonal extracts vital information from the confusion matrix to calculate the evaluative metrics. The main parameters used in the literature are accuracy (Acc), sensitivity (Sen), specificity (Spe) and positive predictive values (PPV).

The accuracy is the ratio of true items (positives and negatives) for the entire population and represents the percentage of positive and negative samples correctly classified. The specificity is the ratio between negative samples correctly identified over all negative samples. The positive predictive value is the proportion between the items correctly classified and all items belonging to a class. Sensitivity measures the proportion of items correctly classified among all true classifications.

3. Materials and methods

In this section, the chemical composition of the materials, the manufacturing processes of the samples, the metallographic preparation of the samples and the computational methodology used are presented. Fig. 6 shows the process adopted from the acquisition of the material to the classification.

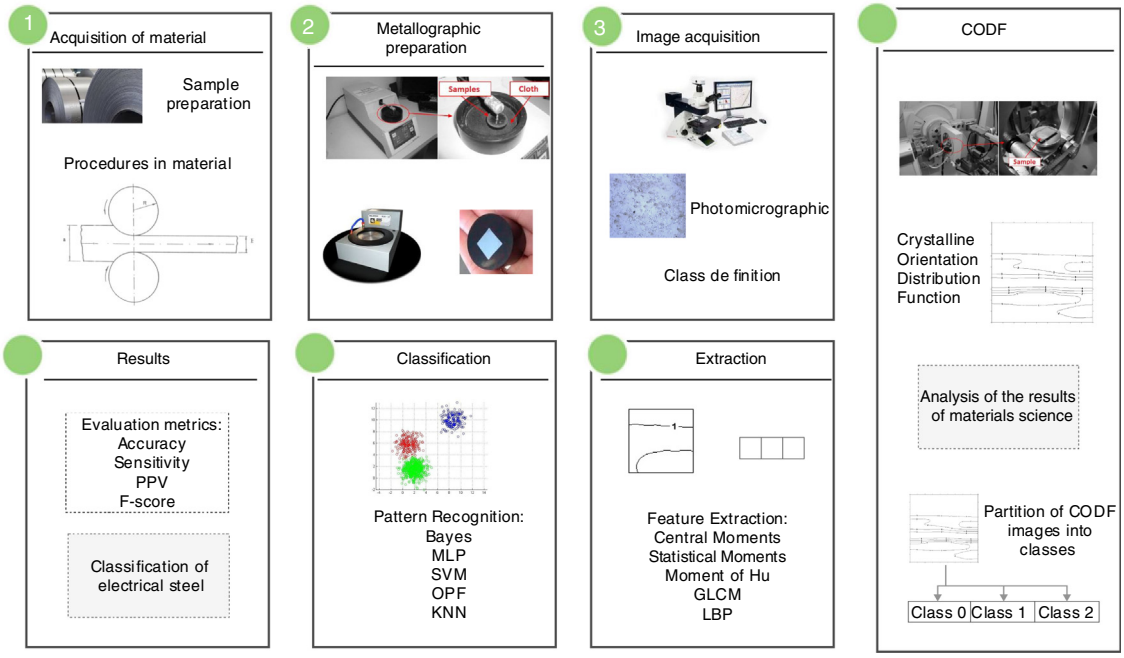

Fig. 6 – The procedures adopted in this study.

Table 1 – The chemical composition of the semi-processed NGO electrical steel.

Element	% (mass)
Carbon (C)	0.050
Manganese (Mn)	0.029
Silicon (Si)	1.280
Phosphorus (P)	0.025
Sulfur (S)	0.014
Aluminum (Al)	0.036
Niobium (Nb)	–
Titanium (Ti)	–
Boron (B)	–
Vanadium (V)	–

Table 2 – The manufacturing procedures of the samples for each class.

Class	Reductions	Temperature	Time
Class 0	50%	620 °C	1, 10, 100 and 1000 min
		730 °C	1, 10, 100 and 1000 min
	70%	620 °C	1, 10, 100 and 1000 min
		730 °C	1, 10, 100 and 1000 min
Class 1	50%	840 °C	1, 10 and 100 min
		900 °C	1 and 10 min
	70%	840 °C	1 and 10 min
Class 2	50%	840 °C	1000 min
		900 °C	100 and 1000 min
	70%	840 °C	100 and 1000 min
		900 °C	1, 10, 100 and 1000 min

3.1. *Materials*

The materials correspond to portions of semi-processed NGO electrical steel sheets that measure 60 mm × 40 mm. Table 1 shows the chemical composition.

Samples were annealed at 730 °C for 12 h and cold-rolled to thickness reductions of 50% (1.2 mm thick) and 70% (0.6 mm thick). For secondary recrystallization, these samples were subjected to post-heat treatments at temperatures of 620 °C, 730 °C, 840 °C and 900 °C, and were maintained at each temperature for 1, 10, 100 and 1000 min.

The samples were then immersed in a solution of 5% hydrofluoric acid and 95% hydrogen peroxide for about five seconds and then placed under running water to remove any excess solution. This acid treatment aims at alleviating the surface tensions of the region to be analyzed.

X-ray diffraction was used to acquire images of the CODF. Cobalt (λ 1.7890 Å) and Molybdenum (λ 0.7093 Å) radiations were used, respectively, on the laminated samples, reduced by 50% and 70%, submitted to the heat treatment for grain growth.

DATA COLLECTOR software was used for the acquisition of the data to obtain the pole figures. The software POPLA processed these images and produced the CODF. The CODF plot was via the SURFER software.

The 32 images of the database were divided into three distinct classes. The criterion for this division was the evolution of the microstructural state of the material, in which the CODF image corresponds. Table 2 shows the manufacturing procedures of the samples for each class.

The metallographic images were collected using an optical microscope (Zeiss) with digital image acquisition, and original magnification ×100. All images had a resolution of 2436 × 2042 pixels.

Class 0 exhibited no changes in its microstructure when the microstructural state was compared with the annealed samples at 730 °C for 12 h. Class 1 showed a considerable grain growth compared to Class 0. These are grains with normal

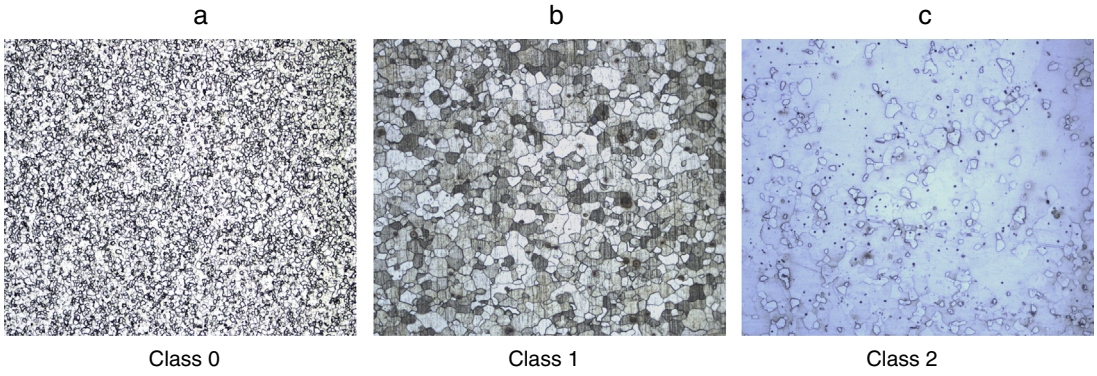

Fig. 7 – Photomicrographs of samples.

growth generated by primary recrystallization. The samples from Class 2, showed an abnormal grain growth, characteristic of the secondary recrystallization phenomenon. Class 2 represents the state of highest electromagnetic efficiency of the material. Fig. 7 shows examples for each class.

3.2. *Computational methodology*

The CODF images were then submitted to feature extractors. Table 3 shows all the methods used in this step, as well as their respective number of attributes.

The original training and test samples were shuffled and randomly divided into two sets, where 50% of the data of each class was selected for training data and 50% for testing. Five iterations were used to obtain the computational results.

Table 3 – Number of attributes generated by each extractor.

Feature extraction	Number of attributes
Statistical Moments	10
Central Moments	7
Hu's Moments	7
Gray Level Co-occurrence Matrix (GLCM)	14
Local Binary Patterns (LBP)	48

The computational performance and efficacy of the proposed method were evaluated with computational simulations using the following classifiers and their variations: the MLP settings were 10/10/11 and 10/14/11 representing the number of neurons in the input, hidden, and output

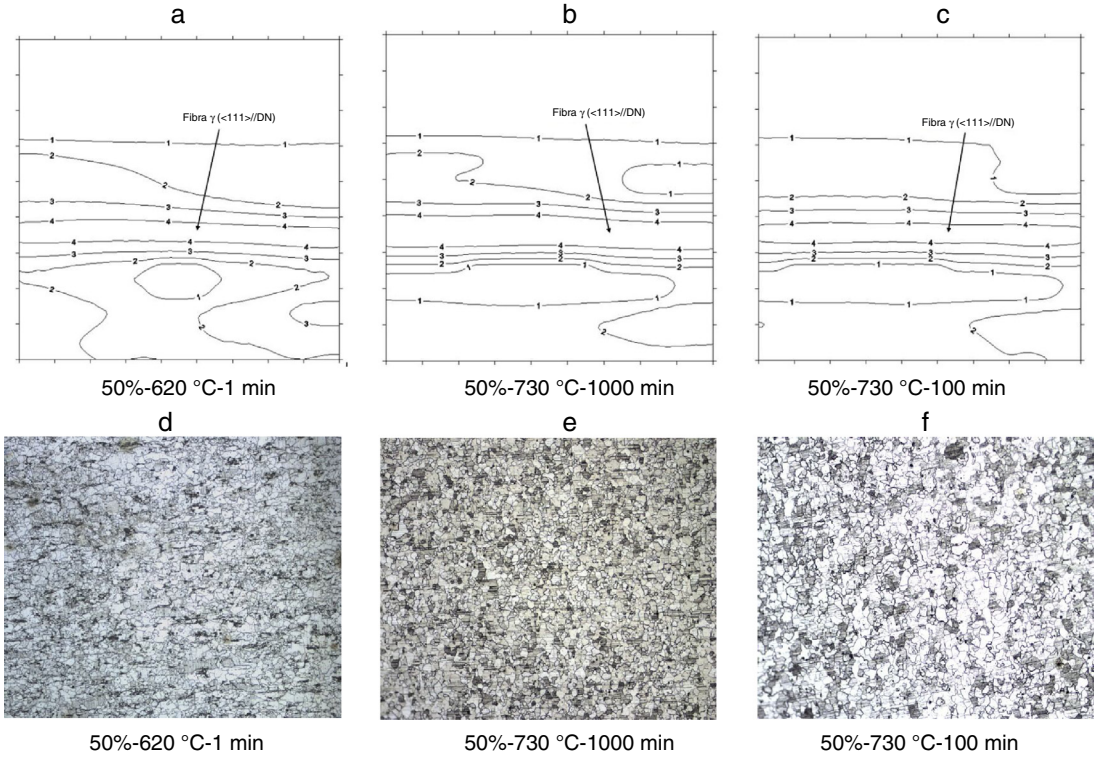

Fig. 8 – CODF of Class 0 and the respective photomicrographs of the samples.

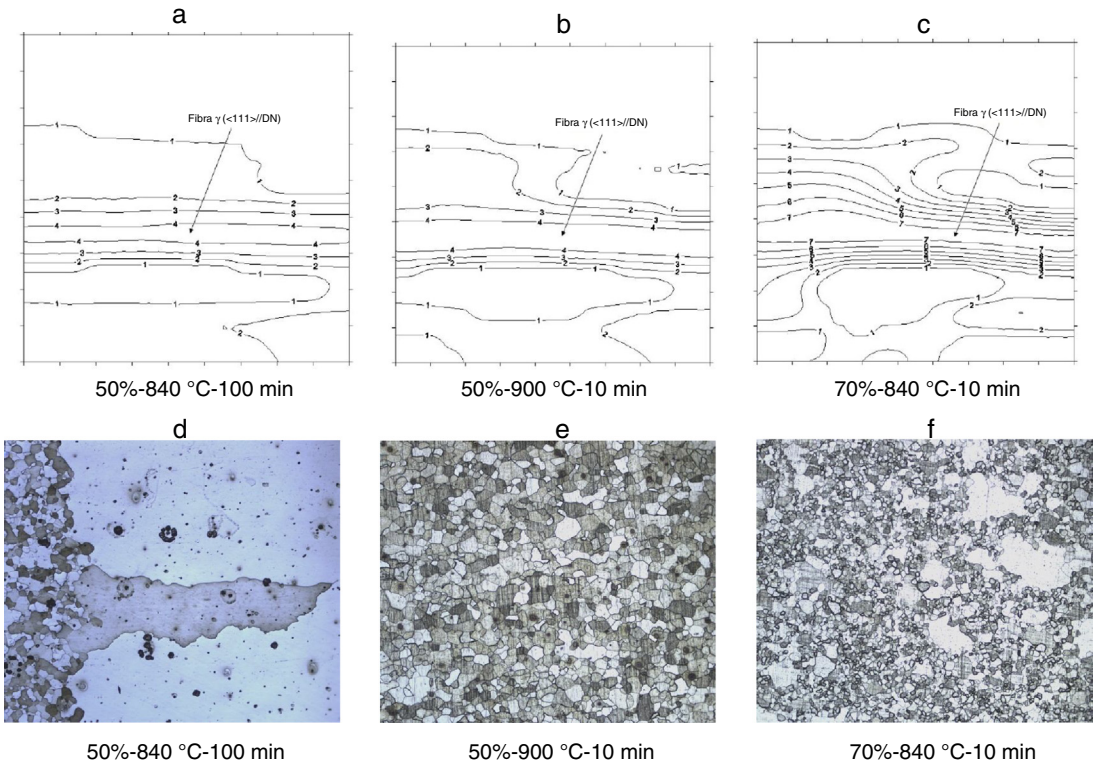

Fig. 9 – CODF of Class 1 and the respective photomicrographs of the samples.

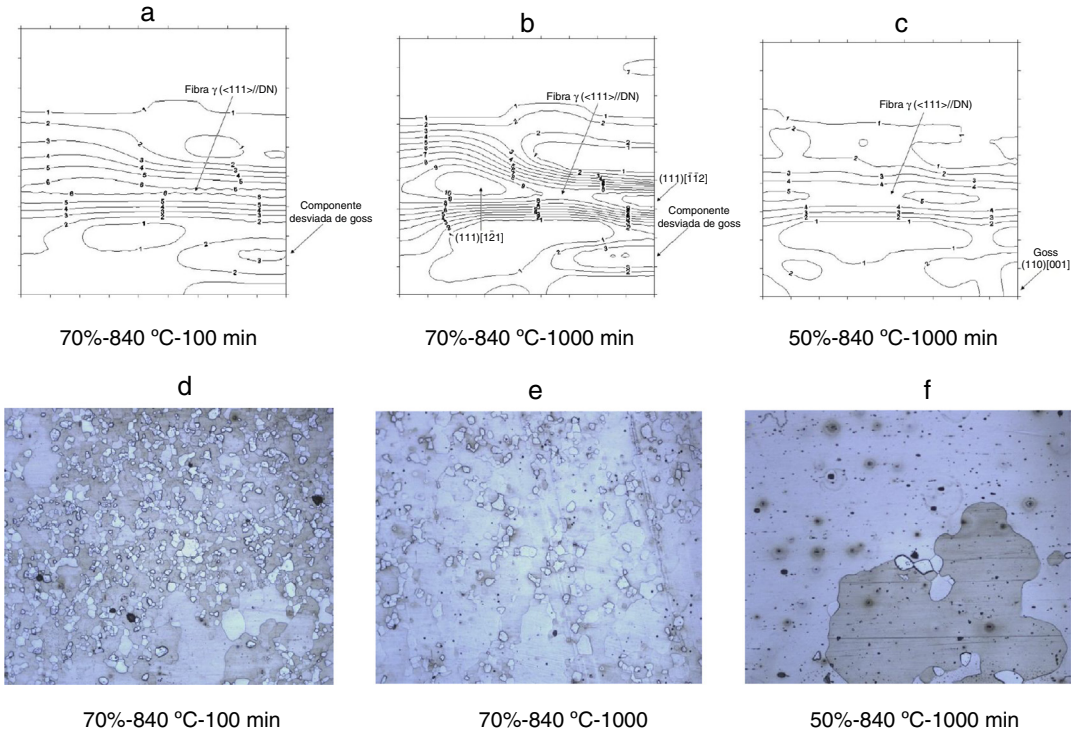

Fig. 10 – CODF of Class 2 and the respective photomicrographs of the samples.

layers, respectively; kNN with 1, 3 and 5 neighbors; Bayesian; SVM with kernels linear, polynomial, RBF and sigmoid; and the OPF with the distances Braycurtis, Canberra, Euclidean, and Squared-Chi-Squared. The SVM used here automatically performs the search for optimal parameters during training.

The validation of the applied models was performed using the evaluation metrics for the classifiers, such as accuracy,

Table 4 – Metrics obtained by feature extraction and classifiers in a virtual environment.

Extractors	Classifiers	Setup	Specificity (%)	Sensitivity (%)	PPV (%)	Accuracy (%)
	Bayes	Normal	69.14 ± 0.00	57.06 ± 0.00	79.57 ± 0.00	73.32 ± 0.00
	SVM	Linear	79.15 ± 0.00	62.94 ± 0.00	84.00 ± 0.00	79.13 ± 8.814
		RBF	69.78 ± 0.00	57.06 ± 0.00	67.14 ± 0.00	71.59 ± 0.00
		Polynomial	86.93 ± 0.00	80.69 ± 0.00	80.34 ± 0.00	89.00 ± 0.00
		Sigmoid	62.94 ± 0.00	57.06 ± 0.00	74.00 ± 4.89	70.90 ± 0.00
GLCM	OPF	Braycurtis	88.69 ± 0.00	62.94 ± 0.00	61.19 ± 0.00	76.09 ± 0.00
		Canberra Euclidean	80.47 ± 0.00	67.65 ± 0.98	66.08 ± 0.00	79.76 ± 0.00
		Squared-Chi-Squared	78.64 ± 0.00	62.94 ± 0.00	69.93 ± 0.00	76.64 ± 0.00
			82.79 ± 0.00	60.59 ± 0.00	61.33 ± 9.54	75.81 ± 0.00
	MLP	10/10/11	78.94 ± 0.00	58.24 ± 0.00	68.13 ± 0.00	74.64 ± 0.00
		10/14/11	76.25 ± 0.00	55.88 ± 0.00	80.00 ± 0.00	74.93 ± 0.00
	KNN	N = 1	80.89 ± 0.00	57.06 ± 0.00	54.99 ± 0.00	72.28 ± 0.00
		N = 3	69.78 ± 0.00	57.06 ± 0.00	53.42 ± 0.00	71.25 ± 0.00
		N = 5	60.93 ± 0.00	39.41 ± 0.00	50.00 ± 0.00	58.44 ± 0.00
	Bayes	Normal	76.62 ± 0.00	57.06 ± 0.00	71.52 ± 0.00	76.78 ± 0.00
	SVM	Linear	85.47 ± 0.00	74.71 ± 0.00	73.46 ± 0.00	8578 ± 0.00
		RBF	62.94 ± 0.00	57.06 ± 0.00	74.00 ± 0.00	70.90 ± 0.00
		Polynomial Sigmoid	85.47 ± 0.00	74.71 ± 0.00	73.46 ± 0.00	76.21 ± 0.34
			62.94 ± 0.00	57.06 ± 0.00	74.00 ± 0.00	70.90 ± 0.00
LPB	OPF	Braycurtis	90.38 ± 0.00	74.71 ± 0.00	82.35 ± 0.00	87.85 ± 0.00
		Canberra Euclidean	89.38 ± 0.00	71.18 ± 0.00	69.42 ± 0.00	83.29 ± 0.00
		Squared-Chi-Squared	83.86 ± 0.00	80.59 ± 0.00	77.32 ± 0.00	88.55 ± 0.00
			89.69 ± 0.00	79.41 ± 0.00	79.10 ± 0.00	87.72 ± 0.00
	MLP	10/10/11	89.80 ± 1.33	75.88 ± 0.00	76.29 ± 0.00	86.61 ± 1.61
		10/14/11	91.36 ± 1.96	77.06 ± 0.00	79.41 ± 0.00	88.55 ± 3.12
	KNN	N = 1	78.43 ± 0.00	62.94 ± 0.00	59.98 ± 0.00	76.78 ± 0.00
		N = 3	68.17 ± 0.00	62.94 ± 0.00	67.67 ± 0.00	75.40 ± 0.00
		N = 5	75.09 ± 0.00	67.65 ± 0.00	71.52 ± 0.00	80.10 ± 1.23
	Bayes	Normal	52.94 ± 0.00	57.06 ± 0.00	64.00 ± 0.00	60.90 ± 0.00
	SVM	Linear	60.95 ± 0.00	52.94 ± 0.00	69.57 ± 0.00	66.44 ± 0.00
		RBF	58.94 ± 0.00	52.94 ± 0.00	57.67 ± 0.00	75.05 ± 0.00
		Polynomial Sigmoid	72.52 ± 8.30	57.65 ± 0.00	53.39 ± 0.00	70.89 ± 0.00
			52.94 ± 0.00	47.65 ± 0.00	64.00 ± 0.00	60.90 ± 0.00
Central Moments	OPF	Braycurtis	61.71 ± 0.00	45.29 ± 0.00	45.42 ± 0.00	63.94 ± 0.00
		Canberra Euclidean	76.43 ± 0.00	68.82 ± 0.00	68.82 ± 0.00	71.63 ± 0.00
		Squared-Chi-Squared	70.27 ± 0.00	58.24 ± 0.00	59.70 ± 0.00	73.69 ± 0.00
			67.02 ± 0.00	48.24 ± 0.00	76.67 ± 0.00	73.81 ± 0.00
	MLP	10/10/11	79.50 ± 0.00	70.59 ± 0.00	77.89 ± 0.00	79.93 ± 0.00
		10/14/11	79.42 ± 0.00	68.82 ± 0.00	68.01 ± 0.00	72.80 ± 0.00
	KNN	N = 1	79.21 ± 0.00	68.82 ± 0.00	68.74 ± 0.34	71.28 ± 0.00
		N = 3	67.97 ± 0.00	51.18 ± 0.00	49.22 ± 0.00	67.09 ± 0.00
		N = 5	62.94 ± 0.00	57.06 ± 0.00	74.00 ± 0.00	70.90 ± 0.00
	Bayes	Normal	71.20 ± 0.00	61.96 ± 0.00	51.45 ± 0.09	79.90 ± 0.00
	SVM	Linear	68.17 ± 0.00	62.94 ± 0.00	77.67 ± 0.00	75.40 ± 0.00
		RBF	68.17 ± 0.00	62.94 ± 0.00	76.67 ± 0.00	75.40 ± 0.00
		Polynomial Sigmoid	70.95 ± 0.00	62.94 ± 0.00	79.57 ± 0.00	76.44 ± 0.00
			62.94 ± 0.00	57.06 ± 0.00	74.00 ± 0.00	70.90 ± 0.00
Hu's Moments	OPF	Braycurtis	68.17 ± 0.00	62.94 ± 0.00	76.67 ± 0.00	75.40 ± 0.00
		Canberra Euclidean	77.14 ± 0.00	62.94 ± 0.00	73.16 ± 0.00	76.78 ± 0.00
		Squared-Chi-Squared	73.96 ± 0.00	39.41 ± 0.00	40.77 ± 0.00	60.52 ± 0.00
			69.78 ± 0.00	57.06 ± 0.00	73.64 ± 0.00	72.63 ± 0.00
	MLP	10/10/11	73.40 ± 0.00	68.82 ± 0.00	79.57 ± 0.00	79.90 ± 0.00
		10/14/11	75.49 ± 0.00	71.18 ± 0.00	70.83 ± 1.34	71.56 ± 0.00
	KNN	N = 1	71.67 ± 0.00	62.94 ± 0.00	63.78 ± 0.00	79.90 ± 0.00
		N = 3	58.48 ± 0.00	33.53 ± 0.00	50.00 ± 0.00	55.33 ± 0.01
		N = 5	76.86 ± 0.00	71.18 ± 0.00	72.09 ± 0.00	72.25 ± 4.29
	Bayes	Normal	78.63 ± 0.00	33.53 ± 0.00	75.00 ± 0.00	74.39 ± 0.00
	SVM	Linear	63.40 ± 0.00	68.82 ± 0.34	79.57 ± 0.00	79.90 ± 0.01
		RBF	75.15 ± 0.00	68.82 ± 0.00	67.10 ± 0.00	71.97 ± 0.00
		Polynomial Sigmoid	70.49 ± 0.00	73.53 ± 0.00	75.50 ± 0.00	74.60 ± 1.64
			62.94 ± 0.00	57.06 ± 0.00	74.00 ± 0.00	70.90 ± 0.00

– Table 4 (*Continued*)

Extractors	Classifiers	Setup	Specificity (%)	Sensitivity (%)	PPV (%)	Accuracy (%)
Statistical Moments	OPF	Braycurtis	62.94 ± 0.00	57.06 ± 0.00	74.00 ± 0.00	70.90 ± 0.00
		Canberra Euclidean	1759.13 ± 0.00	45.29 ± 0.00	70.00 ± 0.00	65.71 ± 0.00
		Squared-Chi-Squared	72.05 ± 0.00	74.71 ± 0.00	72.84 ± 0.00	74.39 ± 0.00
			79.74 ± 0.00	74.71 ± 0.00	75.00 ± 0.00	76.47 ± 0.00
	MLP	10/10/11	77.18 ± 0.00	68.82 ± 0.00	72.73 ± 0.00	70.93 ± 0.00
		10/14/11	70.75 ± 0.00	71.18 ± 0.00	74.45 ± 0.00	73.29 ± 2.89
	KNN	$N = 1$	60.62 ± 0.00	33.53 ± 0.00	43.33 ± 0.00	54.98 ± 0.00
		$N = 3$	71.59 ± 0.00	62.94 ± 0.00	57.59 ± 0.00	75.40 ± 0.00
		$N = 5$	68.41 ± 0.00	47.06 ± 0.00	78.41 ± 1.42	73.11 ± 0.68

sensitivity, specificity and PPV. The work developed here does not state if an extractor-classifier combination is better or worse than another, it only answers which are the most suitable for this application.

The results generated by the computational classification system were also compared to the results produced by the traditional methods of analysis performed by a specialist. This specialist used photomicrographs to determine the electromagnetic performance of the electric steel under study.

4. Results

The results of this study are divided into two subsections: first, the results related to the study and analysis of the materials through their respective CODF images and the photomicrographs, and second, the computational results for the classification of electrical steel from the CODF images.

4.1. *Results of materials science*

The Class 0 samples did not present any significant changes in their microstructure when compared to the material without treatment. The size of the grains after treatment was much lower than the ideal defined by [13]. The crystallographic texture of these samples can be observed in Fig. 8a–c. The figures exhibit the sections of $\phi_2 = 45^\circ$ only for the formation of fiber γ ($\langle 111 \rangle$//DN). There is no Goss Component in Class 0.

The photomicrographs of Fig. 9d–f correspond to Class 1 and reveal considerable grain growth compared to the Class 0 samples in Fig. 8d–f. In Class 1 the grains are uniform and equiaxial. Thus, the increase in temperature and annealing time is directly related to increasing the grain size of the samples of this class.

Fig. 9a–c present the CODF in the sections of $\phi_2 = 45^\circ$. An analysis of its crystallographic texture reveals only the formation of the fiber γ ($\langle 111 \rangle$//DN). Still without the formation of the Goss component which characterizes secondary recrystallization.

Fig. 10d–f belongs to Class 2. Samples of this class show an abnormal growth of some grains. This phenomenon is called secondary recrystallization and it is the result of a deviation from the conventional grain growth pattern that occurs when the microstructure becomes unstable, and growth occurs only in a small number of grains. The remaining grains of the sample remain unchanged until grains with abnormal growth consume them. The secondary recrystallization is the result of the increase in temperature and annealing time.

The analysis of the crystallographic texture of Class 2 is through Fig. 10a–c. Their CODF show the appearance of component (110) [001] on the right and bottom side of each CODF. The formation of this component coincides with the onset of secondary recrystallization.

The thermal treatment at 840 °C for 1000 min shows the formation of component (110) [001] (Fig. 10c), with intensity 3 and the structure of this component coincides precisely in the heat treatment in which the phenomenon of abnormal grain growth was observed through the photomicrography in Fig. 10f.

4.2. *Computational results*

All methodologies were implemented in C/C++ using Visual Studio 2012. In addition, this study used the OpenCV 3.0 and the computational process was performed on a computer with a Mac X El Capitan 10.11.2 operational system, Intel Core i5 processor with 2.4 GHz and 8 GB RAM.

Table 4 shows the average and standard deviation values for accuracy, sensitivity, positive predictive value (PPV) and specificity from the classifiers based on Bayes, MLP, kNN, OPF, and SVM, using the five extractors.

The results in Table 4 show that the most accurate is the GLCM extractor combined with the SVM classifier using the polynomial kernel (89.00%). The LBP also presented good accuracy results with the OPF classifier using the Euclidean distance (88.55%) and with the MLP-10/14/11 (88.55%), OPF with the distance Braycurtis (87.85%), followed by OPF with Squared-Chi-Squared distance (87.72%), MLP with 10 input neurons, 10 hidden neurons and 11 neurons in the output (86.61%), SVM with Linear kernel (85.78%), OPF with Canberra (83.29%), and KNN with κ equal to 5 (80.10%). The percentage values of the sensitivity, specificity, and PPV metrics presented in Table 4 reaffirm the reliability of the values shown in the accuracy of the extractor-classifier combinations. The confidence interval used was 95%.

The accuracy results in Table 4 for Hu's Moments, Central Moments and Statistical Moments were lower compared to the GLCM and LBP extractors. These results are justified as these extractors acquire information about the shapes of the objects, which is a complication due to the similarity in the formats between the CODF of the classes.

The best results achieved by each classifier are shown in Table 5, detailing the training, testing and total times. Also, the GLCM and LBP extraction time is displayed. By making a direct comparison between the two extractors that obtained the best

Table 5 – The extraction time, training time (TrT), testing time (Tst) and total time (TT) for all feature extractions obtained by the best classifiers.

Extractor	Classifier	TrT(s)	TsT(s)	TtT(s)	Extraction time (s)
GLCM	SVM (Polynomial)	0.000600 ± 0.000490	0.00 ± 0.00	0.000600	0.230
	OPF (Euclidean)	0.000200 ± 0.000400	0.00 ± 0.00	0.000200	
	MLP (10/14/11)	0.049000 ± 0.032094	0.00 ± 0.00	0.049000	
	OPF (Braycurtis)	0.000300 ± 0.000400	0.00 ± 0.00	0.000300	
	OPF (Squared-Chi-Squared)	0.000800 ± 0.000400	0.001600 ± 0.001506	0.002400	
LBP	MLP (10/10/11)	0.035000 ± 0.007014	0.00 ± 0.00	0.035000	0.120
	SVM (Linear)	0.005000 ± 0.000001	0.00 ± 0.00	0.005000	
	OPF (Canberra)	0.000450 ± 0.000000	0.00 ± 0.00	0.0004500	
	KNN ($\kappa = 5$)	0.010000 ± 0.000001	0.00 ± 0.00	0.010000	

results in the classification metrics, the LBP extractor, even with a much more significant number of attributes extracted, was two times faster than the GLCM extractor.

Another analysis is based on the confusion matrix presented in Table 6, which depicts the classes under study and the classification results obtained according to the classifier and the feature extraction methods used.

As presented in this article, the best extractor in [18] was GLCM. However, in [18] the best extractor had the highest values of accuracy with the classifier kNN with κ equal to 1, while in this article the highest values were achieved with the SVM classifier and the Polynomial kernel. Although the values of the evaluative metrics in [18] are slightly higher than those presented in this article, where the classification

Table 6 – Average confusion matrices for 5 runs using the best classifiers under comparison applied to the features extracted using the GLCM and LBP methods.

True class	Classified as	SVM – Polynomial (GLCM)	OPF – Euclidean (LBP)	MLP – 10/14/11 (LBP)
Class 1	Class 1	3.4	2.0	6.8
	Class 2	0.0	1.0	3.2
	Class 3	0.0	1.5	2.6
Class 2	Class 1	1.2	3.0	0.0
	Class 2	3.2	5.0	4.5
	Class 3	0.0	1.0	0.0
Class 3	Class 1	0.0	1.0	1.2
	Class 2	0.1	0.0	0.8
	Class 3	2.9	2.0	2.4

True class	Classified as	OPF – Braycurtis (LBP)	OPF – Squared-Chi-Squared (LBP)	MLP – 10/10/11 (LBP)
Class 1	Class 1	6.0	7.0	6.8
	Class 2	3.0	3.0	3.0
	Class 3	2.0	5.0	2.4
Class 2	Class 1	0.0	1.0	1.0
	Class 2	1.0	0.2	0.6
	Class 3	0.0	0.0	0.6
Class 3	Class 1	2.0	0.0	0.2
	Class 2	0.0	0.0	0.4
	Class 3	3.0	1.0	1.0

True class	Classified as	SVM – Linear (LBP)	OPF – Canberra (LBP)	KNN – $\kappa = 5$ (LBP)
Class 1	Class 1	3.0	4.0	8.0
	Class 2	1.2	2.4	4.0
	Class 3	1.4	2.6	5.0
Class 2	Class 1	3.0	2.8	0.3
	Class 2	1.0	1.6	0.7
	Class 3	0.4	0.0	0.4
Class 3	Class 1	0.0	0.0	0.0
	Class 2	0.9	1.2	0.6
	Class 3	1.6	2.4	1.2

methodology of the electric steel was based on the crystallographic texture.

The computational results were coherent with the specialist's results, confirming again that the study conducted here is suitable to evaluate the performance of the electromagnetic effects of a material through the CODF.

5. Conclusion

The present work presents an innovative methodology for the classification of non-grain oriented electrical steel in terms of its electromagnetic efficiency. Traditionally this classification is performed by a thorough analysis of the CODF images and the hysteresis curves. This study successfully developed, implemented, and tested a computational solution with a high percentage of accuracy and reliability in the classification of these electrical steels. Only the analysis of the CODF images were used, and the results superseded the limitations related to the general study carried out by specialists. This work also presented, as a significant contribution, a rapid and precise automation of this classification process.

The best result for classification accuracy was the GLCM extractor combined with the SVM classifier and the polynomial kernel. The evaluation metrics for this model were 89.00% accuracy, 86.93% specificity, the sensitivity of 80.69% and PPV of 80.34%.

The authors concluded that the model is useful, within the accepted tolerance range, for use at an academic level by students, engineers, researchers and specialists in the areas of renewable energy with a focus on energy efficiency, engineering and materials science. Consequently, it may be considered a viable, reliable and fast option for obtaining accurate classification results.

Conflicts of interest

The authors declare no conflicts of interest.

REFERENCES

[1] Zuo H, Ai D. Environment, energy and sustainable economic growth. Procedia Eng 2011;21:513–9, http://dx.doi.org/10.1016/j.proeng.2011.11.2045.

[2] Laha P, Chakraborty B. Energy model – a tool for preventing energy dysfunction. Renew Sustain Energy Rev 2017;73:95–114, http://dx.doi.org/10.1016/j.rser.2017.01.106.

[3] de Araujo Cardoso RF, da Cunha MA, Brandão LPM. Optimization of the magnetic losses of electrical steels through addition of Al and Si using a hot dipping process. J Mater Res Technol 2013;2(3):276–81, http://dx.doi.org/10.1016/j.jmrt.2013.02.014.

[4] Wang H, Zhang Y, Li S. Laser welding of laminated electrical steels. J Mater Process Technol 2016;230:99–108, http://dx.doi.org/10.1016/j.jmatprotec.2015.11.018.

[5] Sugawara Y, Akatsu K. Characteristics of a switched reluctance motor using grain-oriented electric steel sheet. In: 2013 International Conference on Electrical Machines and Systems (ICEMS). 2013. p. 18–23, http://dx.doi.org/10.1109/ICEMS.2013.6754544.

[6] Qin J, Yang P, Mao W, Ye F. Effect of texture and grain size on the magnetic flux density and core loss of cold-rolled high silicon steel sheets. J Magn Magn Mater 2015;393:537–43, http://dx.doi.org/10.1016/j.jmmm.2015.06.032.

[7] Hilinski EJ, Johnston GH. Annealing of electrical steel. In: 2014 4th International Electric Drives Production Conference (EDPC). 2014. p. 1–7, http://dx.doi.org/10.1109/EDPC.2014.6984385.

[8] Hubert O, Daniel L, Billardon R. Experimental analysis of the magnetoelastic anisotropy of a non-oriented silicon iron alloy. Proceedings of the 15th International Conference on Soft Magnetic Materials (SMM15). J Magn Magn Mater 2003;254–255:352–4, http://dx.doi.org/10.1016/S0304-8853(02)00850-8.

[9] da Silva FE, Freitas FNC, Abreu HFG, Gonçalves LL, de Moura EP, Silva Daniel MR. Characterization of the evolution of recrystallization by fluctuation and fractal analyses of the magnetic hysteresis loop in a cold rolled non-oriented electric steel. J Mater Sci 2011;46(10):3282–90, http://dx.doi.org/10.1007/s10853-010-5215-8.

[10] Xia Z, Kang Y, Wang Q. Developments in the production of grain-oriented electrical steel. J Magn Magn Mater 2008;320(23):3229–33, http://dx.doi.org/10.1016/j.jmmm.2008.07.003.

[11] Sorrell S. Reducing energy demand: a review of issues, challenges and approaches. Renew Sustain Energy Rev 2015;47:74–82, http://dx.doi.org/10.1016/j.rser.2015.03.002.

[12] Bohn F, Gündel A, Landgraf F, Severino A, Sommer R. Magnetostriction in non-oriented electrical steels. lAW3M-05 Proceedings of the Seventh Latin American Workshop on Magnetism, Magnetic Materials and their Applications. Physica B: Condensed Matter 2006;384(1–2):294–6, http://dx.doi.org/10.1016/j.physb.2006.06.014.

[13] Shimanaka H, Ito Y, Matsumara K, Fukuda B. Recent development of non-oriented electrical steel sheets. J Magn Magn Mater 1982;26(1):57–64, http://dx.doi.org/10.1016/0304-8853(82)90116-0.

[14] Liu H-T, Wang Y-P, An L-Z, Wang Z-J, Hou D-Y, Chen J-M, et al. Effects of hot rolled microstructure after twin-roll casting on microstructure, texture and magnetic properties of low silicon non-oriented electrical steel. J Magn Magn Mater 2016;420:192–203, http://dx.doi.org/10.1016/j.jmmm.2016.07.034.

[15] Salinas-Beltrán J, Salinas-Rodríguez A, Gutérrez-Castañeda E, Lara RD. Effects of processing conditions on the final microstructure and magnetic properties in non-oriented electrical steels. J Magn Magn Mater 2016;406:159–65, http://dx.doi.org/10.1016/j.jmmm.2016.01.017.

[16] Fang F, Xu Y-B, Zhang Y-X, Wang Y, Lu X, Misra R, et al. Evolution of recrystallization microstructure and texture during rapid annealing in strip-cast non-oriented electrical steels. J Magn Magn Mater 2015;381:433–9, http://dx.doi.org/10.1016/j.jmmm.2015.01.026.

[17] Bertotti G. Connection between microstructure and magnetic properties of soft magnetic materials. Proceedings of the 18th International Symposium on Soft Magnetic Materials. J Magn Magn Mater 2008;320(20):2436–42, http://dx.doi.org/10.1016/j.jmmm.2008.04.001.

[18] Filho PPR, dos Santos JC, Freitas FNC, de Araújo Rodrigues D, Ivo RF, Herculano LFG, et al. New approach to evaluate a non-grain oriented electrical steel electromagnetic performance using photomicrographic analysis via digital image processing. J Mater Res Technol 2017, http://dx.doi.org/10.1016/j.jmrt.2017.09.007.

[19] Chwastek KR, Baghel APS, de Campos MF, Kulkarni SV, Szczygłowski J. A description for the anisotropy of magnetic properties of grain-oriented steels. IEEE Trans Magn

2015;51(12):1–5, http://dx.doi.org/10.1109/TMAG.2015.2449775.
[20] Freitas FN, da Silva MR, Tavares SS, Abreu HF. Texture and microstructure evolution during box annealing of a non-oriented-grain electrical steel. In: Textures of materials – ICOTOM 16. Materials science forum, vol. 702. Trans Tech Publications; 2012. p. 595–8, http://dx.doi.org/10.4028/www.scientific.net/MSF.702-703.595.
[21] de Albuquerque VHC, Cortez PC, de Alexandria AR, Tavares JMR. A new solution for automatic microstructures analysis from images based on a backpropagation artificial neural network. Nondestructive Test Eval 2008;23(4):273–83, http://dx.doi.org/10.1080/10589750802258986.
[22] Albuquerque VHCD, Tavares JMR, Cortez PC. Quantification of the microstructures of hypoeutectic white cast iron using mathematical morphology and an artificial neural network. Int J Microstruct Mater Prop 2010;5(1):52–64, http://dx.doi.org/10.1504/IJMMP.2010.032501.
[23] Rebouças ES, Braga AM, Marques RC, Filho PPR. A new approach to calculate the nodule density of ductile cast iron graphite using a level set. Measurement 2016;89:316–21, http://dx.doi.org/10.1016/j.measurement.2016.04.029.
[24] Burgers W. Principles of recrystallization. In: The art and science of growing crystals. New York: Wiley; 1963. p. 416–50.
[25] Wang X, Liu X, Xie J. Mechanism of surface texture evolution in pure copper strips subjected to double rolling. Prog Nat Sci: Mater Int 2014;24(1):75–82, http://dx.doi.org/10.1016/j.pnsc.2014.01.014.
[26] Salih M, Weidenfeller B, Al-Hamdany N, Brokmeier H-G, Gan W. The effect of intermediate annealing between cold rolled steps on crystallographic texture and magnetic properties of Fe–2.6% Si. J Magn Magn Mater 2014;362:141–9, http://dx.doi.org/10.1016/j.jmmm.2014.03.009.
[27] Pluta WA. Loss components in electrical steel with Goss texture. In: 2013 International Symposium on Electrodynamic and Mechatronic Systems (SELM). 2013. p. 87–8, http://dx.doi.org/10.1109/SELM.2013.6562993.
[28] Na SM, Flatau AB. Surface-energy-induced selective growth of (001) grains in magnetostrictive ternary Fe–Ga-based alloys. Smart Mater Struct 2012;21(5):055024.
[29] Filho PPR, Moreira FDL, Xavier FGdL, Gomes SL, Santos JCd, Freitas FNC, et al. New analysis method application in metallographic images through the construction of mosaics via speeded up robust features and scale invariant feature transform. Materials 2015;8(7):3864–82, http://dx.doi.org/10.3390/ma8073864.
[30] Jain AK, Duin RPW, Mao J. Statistical pattern recognition: a review. IEEE Trans Pattern Anal Mach Intell 2000;22(1):4–37, http://dx.doi.org/10.1109/34.824819.
[31] Xiankang L, Meiguo G, Xiongjun F. Application of HRRP even rank central moments features in satellite target recognition. In: 2007 IET International Conference on Radar Systems. 2007. p. 1–4, http://dx.doi.org/10.1049/cp:20070620.
[32] Lai R, Liu X, Ohkawa F. A fast template matching algorithm based on central moments of images. In: 2008 International Conference on Information and Automation. 2008. p. 596–600, http://dx.doi.org/10.1109/ICINFA.2008.4608069.
[33] Hu M-K. Visual pattern recognition by moment invariants. IRE Trans Inf Theory 1962;8(2):179–87, http://dx.doi.org/10.1109/TIT.1962.1057692.
[34] Flusser J, Suk T, Boldys J, Zitova B. Projection operators and moment invariants to image blurring. IEEE Trans Pattern Anal Mach Intell 2015;37(4):786–802, http://dx.doi.org/10.1109/TPAMI.2014.2353644.
[35] Licciardi G, Villa A, Dalla Mura M, Bruzzone L, Chanussot J, Benediktsson J. Retrieval of the height of buildings from worldview-2 multi-angular imagery using attribute filters and geometric invariant moments. IEEE J Sel Top Appl Earth Obs Remote Sens 2012;5(1):71–9, http://dx.doi.org/10.1109/JSTARS.2012.2184269.
[36] Yang J, Xiong N, Vasilakos A, Fang Z, Park D, Xu X, et al. A fingerprint recognition scheme based on assembling invariant moments for cloud computing communications. IEEE Syst J 2011;5(4):574–83, http://dx.doi.org/10.1109/JSYST.2011.2165600.
[37] Haralick R. Statistical and structural approaches to texture. Proc IEEE 1979;67(5):786–804, http://dx.doi.org/10.1109/PROC.1979.11328.
[38] Ramalho GLB, Ferreira DS, Rebouças Filho PP, de Medeiros FNS. Rotation-invariant feature extraction using a structural co-occurrence matrix. Measurement 2016;94:406–15.
[39] Neto EC, Cortez PC, Cavalcante TS, da Silva Filho VER, Filho PPR, Holanda MA. Supervised enhancement filter applied to fissure detection. Cham: Springer International Publishing; 2015. p. 337–40, http://dx.doi.org/10.1007/978-3-319-13117-7-87.
[40] Ojala T, Pietikäinen M, Harwood D. A comparative study of texture measures with classification based on featured distributions. Pattern Recogn 1996;29(1):51–9, http://dx.doi.org/10.1016/0031-3203(95)00067-4.
[41] Guo G, Li SZ, Chan K. Face recognition by support vector machines. In: Proceedings Fourth IEEE International Conference on Automatic Face and Gesture Recognition (Cat No. PR00580). 2000. p. 196–201, http://dx.doi.org/10.1109/AFGR.2000.840634.
[42] Vanitha CDA, Devaraj D, Venkatesulu M. Gene expression data classification using support vector machine and mutual information-based gene selection. Procedia Comput Sci 2015;47:13–21, http://dx.doi.org/10.1016/j.procs.2015.03.178.
[43] Furey TS, Cristianini N, Duffy N, Bednarski DW, Schummer M, Haussler D. Support vector machine classification and validation of cancer tissue samples using microarray expression data. Bioinformatics 2000;16(10):906, http://dx.doi.org/10.1093/bioinformatics/16.10.906.
[44] Filho PPR, Sarmento RM, Holanda GB, de Alencar Lima D. New approach to detect and classify stroke in skull CT images via analysis of brain tissue densities. Comput Methods Programs Biomed 2017;148:27–43, http://dx.doi.org/10.1016/j.cmpb.2017.06.011.
[45] Papa JP, de Albuquerque VHC, Falcão AX, Tavares JMRS. Fast automatic microstructural segmentation of ferrous alloy samples using optimum-path forest. Berlin, Heidelberg: Springer Berlin Heidelberg; 2010. p. 210–20, http://dx.doi.org/10.1007/978-3-642-12712-0-19.
[46] de Albuquerque VHC, de Alexandria AR, Cortez PC, Tavares JMR. Evaluation of multilayer perceptron and self-organizing map neural network topologies applied on microstructure segmentation from metallographic images. NDT & E Int 2009;42(7):644–51, http://dx.doi.org/10.1016/j.ndteint.2009.05.002.
[47] Domingos P, Pazzani M. On the optimality of the simple Bayesian classifier under zero-one loss. Mach Learn 1997;29(2):103–30, http://dx.doi.org/10.1023/A:1007413511361.
[48] Islam MJ, Wu QMJ, Ahmadi M, Sid-Ahmed MA. Investigating the performance of naive-Bayes classifiers and k-nearest neighbor classifiers. In: 2007 International Conference on Convergence Information Technology (ICCIT 2007). 2007. p. 1541–6, http://dx.doi.org/10.1109/ICCIT.2007.148.
[49] Ammar A, Bourek A, Benakcha A. Nonlinear SVM-DTC for induction motor drive using input-output feedback linearization and high order sliding mode control. ISA Trans 2017;67:428–42, http://dx.doi.org/10.1016/j.isatra.2017.01.010.
[50] Keskes H, Braham A, Lachiri Z. Broken rotor bar diagnosis in induction machines through stationary wavelet packet transform and multiclass wavelet SVM. Electric Power Syst Res 2013;97:151–7, http://dx.doi.org/10.1016/j.epsr.013.

[51] Vapnik VN. An overview of statistical learning theory. IEEE Trans Neural Netw 1999;10(5):988–99, http://dx.doi.org/10.1109/72.788640.
[52] Duan K-B, Keerthi SS. Which is the best multiclass SVM method? An empirical study. Berlin, Heidelberg: Springer Berlin Heidelberg; 2005. p. 278–85, http://dx.doi.org/10.1007/11494683-28.
[53] Papa JP, Falcão AX, de Albuquerque VHC, Tavares JMR. Efficient supervised optimum-path forest classification for large datasets. Pattern Recogn 2012;45(1):512–20, http://dx.doi.org/10.1016/j.patcog.2011.07.013.
[54] Nunes TM, Coelho AL, Lima CA, Papa JP, de Albuquerque VHC. EEG signal classification for epilepsy diagnosis via optimum path forest – a systematic assessment. Neurocomputing 2014;136:103–23, http://dx.doi.org/10.1016/j.neucom.2014.01.020.
[55] Iwashita A, Papa J, Souza A, Falcão A, Lotufo R, Oliveira V, et al. A path- and label-cost propagation approach to speedup the training of the optimum-path forest classifier. Pattern Recogn Lett 2014;40:121–7, http://dx.doi.org/10.1016/j.patrec.2013.12.018.
[56] de Albuquerque VHC, Barbosa CV, Silva CC, Moura EP, Filho PPR, Papa JP, et al. Ultrasonic sensor signals and optimum path forest classifier for the microstructural characterization of thermally-aged Inconel 625 alloy. Sensors 2015;15(6):12474–97, http://dx.doi.org/10.3390/s150612474.
[57] Ruck DW, Rogers SK, Kabrisky M, Oxley ME, Suter BW. The multi-layer perceptron as an approximation to a Bayes optimal discriminant function. IEEE Trans Neural Netw 1990;1(4):296–8, http://dx.doi.org/10.1109/72.80266.
[58] Cover T, Hart P. Nearest neighbor pattern classification. IEEE Trans Inf Theory 1967;13(1):21–7, http://dx.doi.org/10.1109/TIT.1967.1053964.
[59] Deng Z, Zhu X, Cheng D, Zong M, Zhang S. Efficient kNN classification algorithm for big data. Neurocomputing 2016;195:143–8, http://dx.doi.org/10.1016/j.neucom.2015.08.112.
[60] Aha DW, Kibler D, Albert MK. Instance-based learning algorithms. Mach Learn 1991;6(1):37–66, http://dx.doi.org/10.1007/BF00153759.
[61] Ho TK. Nearest neighbors in random subspaces. Berlin, Heidelberg: Springer Berlin Heidelberg; 1998. p. 640–8, http://dx.doi.org/10.1007/BFb0033288.